Accepted Manuscript

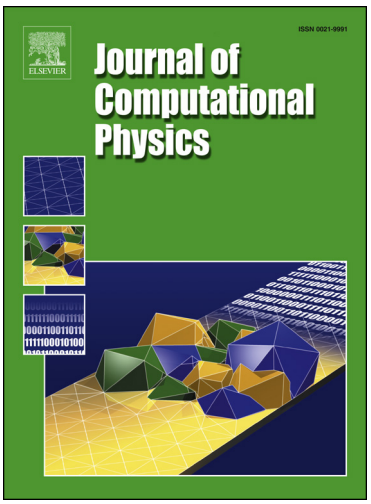

A split-step method to include electron-electron collisions via Monte Carlo in Multiple Rate Equation simulations

Klaus Huthmacher, Andreas K. Molberg, Bärbel Rethfeld, Jeremy R. Gulley

PII: S0021-9991(16)30268-6
DOI: http://dx.doi.org/10.1016/j.jcp.2016.06.043
Reference: YJCPH 6704

To appear in: *Journal of Computational Physics*

Received date: 10 August 2015
Revised date: 22 June 2016
Accepted date: 24 June 2016

Please cite this article in press as: K. Huthmacher et al., A split-step method to include electron-electron collisions via Monte Carlo in Multiple Rate Equation simulations, *J. Comput. Phys.* (2016), http://dx.doi.org/10.1016/j.jcp.2016.06.043

A split-step method to include electron-electron collisions via Monte Carlo in Multiple Rate Equation simulations

Klaus Huthmacher[a], Andreas K. Molberg[b], Bärbel Rethfeld[a], Jeremy R. Gulley[c,*]

[a] *Department of Physics and OPTIMAS Research Center, University of Kaiserslautern*
[b] *Department of Chemistry and OPTIMAS Research Center, University of Kaiserslautern*
[c] *Department of Physics, Kennesaw State University, Kennesaw, GA 30144*

Abstract

A split-step numerical method for calculating ultrafast free-electron dynamics in dielectrics is introduced. The two split steps, independently programmed in `C++11` and `FORTRAN` 2003, are interfaced via the presented open source wrapper. The first step solves a deterministic extended multi-rate equation for the ionization, electron-phonon collisions, and single photon absorption by free-carriers. The second step is stochastic and models electron-electron collisions using Monte-Carlo techniques. This combination of deterministic and stochastic approaches is a unique and efficient method of calculating the nonlinear dynamics of 3D materials exposed to high intensity ultrashort pulses. Results from simulations solving the proposed model demonstrate how electron-electron scattering relaxes the non-equilibrium electron distribution on the femtosecond time scale.

Keywords:
Split-step method, Operator splitting, Laser-induced ionization, Free electron dynamics, Monte Carlo, Electron-electron collisions, `C++11`, `FORTRAN` 2003, interface, `OpenMP`

1. Introduction

Ultrafast laser-material interactions play a critical role for many modern laser applications. In particular, a detailed understanding of laser-induced ionization and many-body effects in dielectrics is necessary for progress in laser machining and ablation [1], laser surgery [2], and laser-induced breakdown spectroscopy [3]. The physics of these applications is strongly nonlinear, and there are few, if any, analytical solutions to problems of general interest [4]. Simulations therefore provide the primary method of theoretical testing for new models for ultrafast laser-material dynamics, as well as for closely related experimental research involving high intensity ultrashort pulse propagation [5–7].

The research areas of laser-material dynamics and pulse propagation are rich in nonlinear physics and can require considerable computational effort to perform comprehensive simulations [6, 8]. This issue is compounded when modeling pulse propagation at high intensities, since the laser field is sufficiently high to ionize the medium through which it propagates. This fact should necessitate a simultaneous and detailed modeling of pulse propagation and free-carrier dynamics, but this is rarely done because of computational constraints. What is typically done instead are calculations of reduced dimensionality [9], or fully 3D models using a highly detailed model of pulse propagation coupled with a greatly simplified model of laser-material dynamics [10], or vice versa [11]. To couple these research areas frequently requires the collaboration of theorists with differing expertise and who program their calculations using different code languages. The occasional need to interface two programming languages for a research collaboration can also have additional

*Corresponding author. Tel.: +1 470 578 2933
Email address: `jgulley@kennesaw.edu` (Jeremy R. Gulley)

computational benefits when one language is particularly well suited to certain calculations or uses scientific libraries unavailable in the language of another collaborator.

In this paper we provide such an interface between code written in `C++11` and `FORTRAN` 2003 code. The simulations performed provide an efficient yet detailed approach to calculate laser-material interactions that are efficient enough to be coupled with pulse propagation simulations in the future. This necessarily involves calculating the free electron distribution as a function of time. Our calculations address this issue by using a split-step method to solve an extended multi-rate equation [12, 13] (EMRE), modeling the free electron distribution as a function of time and electron energy. This method uses the EMRE to model the conduction electron interactions with other particles (photons, phonons, and bound electrons) with simple rate equations coded in `FORTRAN` 2003, while using Monte-Carlo methods to model the computationally intensive electron-electron collisions coded in `C++11` and utilizing freely available `C++11` scientific libraries. The EMRE has been coupled previously to pulse propagation simulations [14], but this did not include direct calculation of the electron-electron scattering, which is typically the dominant influence on the relaxation of the electron distribution on the femtosecond time scale [15].

Using a Monte-Carlo approach to model the dominating influence of electron-electron collisions ensures a representative thermalization of the electron plasma. Our results show how one can efficiently model the evolution of the free-electron energy distribution shape from non-equlibrium to a quasi-equilbrium, *i.e.* a slowly evolving Maxwellian distribution. The results qualitatively capture the evolution occuring on the time-scale of tens of femtoseconds as demonstrated by previous calculations solving the Boltzmann scattering equation for all electron interactions [16].

2. The Extended Multi-Rate Equation

In this section we describe the deterministic step of the calculation. For all simulations in this work the free-electron plasma dynamics are simulated by solving an extended multi-rate equation (EMRE) [13], based on the multiple rate equation (MRE) [12, 18], developed to calculate the electron distribution ρ_e in the conduction band. The EMRE discretizes the energy range of the considered part of the conduction band. As such, n_i describes the electron density in the energy interval $[\epsilon_i, \epsilon_i + \Delta\epsilon]$, i.e., $n_i = \rho_\mathrm{e}(\epsilon_i)\,\Delta\epsilon$, where ϵ_i is the i^th represented conduction-band energy and $\Delta\epsilon$ is the bin width of the energy discretization. Let us stress that $\Delta\epsilon$ is chosen to be the smallest energy transition the model must account for. Finally, the extended multi-rate equation (EMRE) is expressed as

$$\frac{d}{dt} n_i = \dot{n}_i^\mathrm{pi} + \dot{n}_i^\mathrm{imp} + \dot{n}_i^\mathrm{e-pn} + \dot{n}_i^\mathrm{1pht} + \dot{n}_i^\mathrm{e-e}. \tag{1}$$

The terms on the right hand side (RHS) of Eq. (1) describe contributions from photo-ionization, impact ionization, electron-phonon collisions, 1-photon absorption by free-carriers, and electron-electron collisions, respectively. The total electron density n_e as well as the total energy ϵ_tot in the conduction-band are determined according to

$$n_\mathrm{e} = \int_0^{\epsilon_\mathrm{max}} \rho_\mathrm{e}(\epsilon)\,\mathrm{d}\epsilon \qquad \text{and} \qquad \epsilon_\mathrm{tot} = \int_0^{\epsilon_\mathrm{max}} \rho_\mathrm{e}(\epsilon)\,\epsilon\,\mathrm{d}\epsilon\,. \tag{2}$$

Here, ϵ_max is the highest modeled conduction band energy. Below we specify models for these terms. The various energy indices used in these models are summarized in Tab. (1).

Equation (1) is typically solved with standard ODE methods. In this paper we take a combined approach: The last term on the RHS accounting for electron-electron collisions plays a major role in bringing the distribution $\rho_\mathrm{e}(\epsilon)$ from a strongly non-equilibrium configuration to a quasi-equilibrium. It is computationally impractical to simulate this term deterministically. We therefore solve this term with a stochastic method coded in `C++11` and described in Sec. 3. The other processes are coded in `FORTRAN` and are solved with efficient deterministic calculations as described below. The algorithm for these two independent calculations is described in detail in Section 4.

Table 1: Summary of the EMRE indices. The notation $[x]$ denotes the integer part of x.

Index	Definition	Description
i	$[\epsilon_i/\Delta\epsilon]$	Energy index
j	$[\hbar\omega/\Delta\epsilon]$	Photon energy index
m	$[\epsilon^{\max}/\Delta\epsilon]$	Maximum EMRE energy index
s	$[\epsilon^{\rm pn}/\Delta\epsilon]$	Mean phonon energy index
c	$[\epsilon^{\rm crit}/\Delta\epsilon]$	Critical energy index
g	$[\epsilon^{\rm gap}/\Delta\epsilon]$	Band gap energy index
p	$[\epsilon^{\rm pi}/\Delta\epsilon]$	Post photo-ionization energy index
k_l	$[\epsilon_l^{\rm imp}/\Delta\epsilon]$	Post impact-ionization energy index

2.1. Photo-ionization

The photo-ionization term in Eq. (1) is given by [16]

$$\dot{n}_i^{\rm pi} = W^{\rm pi}\left(|E|,\omega\right)\delta_{ip}\ , \tag{3}$$

where we use the Keldysh photo-ionization formula [19] for solids to calculate the photo-ionization probability $W^{\rm pi}\left(\left|E(t)\right|,\omega\right)$, which includes both multi-photon ionization and tunneling contributions. Here, $|E|$ is the electric field amplitude and ω is the optical frequency. The energy at which photo-ionized electrons enter the conduction band is given by

$$\epsilon^{\rm pi} = \left[\tilde{\Delta}/\hbar\omega + 1\right]\hbar\omega - \tilde{\Delta}\ ,$$

where $\tilde{\Delta} = \epsilon^{\rm gap} + q^2\left|E\right|^2/4m_{\rm r}\omega^2$ is the effective band gap [19] comprising the material band gap $\epsilon^{\rm gap}$ and the ponderomotive energy. The reduced-effective mass of the created electron-hole pair is $m_{\rm r}$ and the charge of the electron is q.

2.2. Impact Ionization

The contribution of impact ionization is given by

$$\dot{n}_i^{\rm imp} = -\alpha_i n_i + 2\sum_{l=c}^{m}\delta_{ik_l}\alpha_l n_l\ , \tag{4}$$

where $\alpha(\epsilon_i) = P_{\rm imp}\left((\epsilon_i - \epsilon^{\rm crit})/\epsilon^{\rm crit}\right)^2\theta_{ic}$, is the average energy-dependent impact-ionization rate, where $P_{\rm imp}$ is the impact rate coefficient [16] and θ_{ic} ={1 for $i \geq c$, 0 otherwise} is the step function, $\epsilon^{\rm crit} = \tilde{\Delta}(1+2\mu_{\rm r}^*)/(1+\mu_{\rm r}^*)$ is the critical energy for impact ionization, and $\mu_{\rm r}^*$ is the reduced-effective mass of the conduction and valence electrons. By using a contribution of this form we are following the approach of Ref. [20], albeit extended to an EMRE framework. The approach is designed to conserve both momentum and energy during the impact process. Upon successive absorption events in the conduction band, electrons with energy exceeding the critical energy $\epsilon_i > \epsilon^{\rm crit}$ participate in impact ionization. It collides with a valence electron having a statistical average energy of -$\tilde{\Delta}$/6 below the top of the valence band [20] (the conduction electrons have an energy of $\epsilon_i + \tilde{\Delta}$ relative to the point in energy space). The resulting pair of conduction electrons are assumed to split their energy evenly between them, resulting in an energy of $\epsilon_i^{\rm imp} = (1/2)\epsilon_i - (7/12)\tilde{\Delta}$ when entering the conduction band.

2.3. Electron-Phonon Collisions

The electron-phonon collision term can be approximated by a net plasma energy relaxation into the phonon gas and is given by [13]:

$$\dot{n}_i^{\mathrm{e-pn}} = \frac{n_{i+s}}{\tau_{i+s}^{\mathrm{pn}}} - \frac{n_i}{\tau_i^{\mathrm{pn}}}. \tag{5}$$

Here, τ_i^{pn} is the average energy-dependent electron-phonon scattering time. The scattering time is implemented in terms of the scattering rate ν_i^{pn} and the limits of the energy discretization: $(1/\tau_i^{\mathrm{pn}}) = \nu_i^{\mathrm{pn}}\theta_{is}\theta_{m,i+s}$. In short, the electrons at the energy ϵ_i are assumed to lose an average phonon energy of ϵ^{pn} during a characteristic time τ_i^{pn}.

2.4. Free-Carrier Absorption

The one-photon absorption term on the right hand side of Eq. (1) is given by [20]:

$$\dot{n}_i^{\mathrm{1pht}} = \beta_{i-j} I(t) n_{i-j} - \beta_i I(t) n_i \ . \tag{6}$$

These terms represent the carriers per volume per time entering and leaving the ϵ_{i-j} and ϵ_i energy bins by one-photon absorption, respectively. The optical intensity is $I(t)$ and the formula for the energy dependent coefficient of inverse Bremsstralung absorption β_i is [7]

$$\beta_i = \frac{e^2 \tau_i^{\mathrm{c}}}{m_r n_0 c \epsilon_0 (1 + (\omega \tau_i^{\mathrm{c}})^2)},$$

where n_0 is the linear index of refraction, ω is the optical frequency, and τ_i^{c} is the energy-dependent momentum relaxation time.

3. Electron-electron collisions

In this section we describe how to simulate electron-electron scattering, i.e., the term $\dot{n}_i^{\mathrm{e-e}}$ in Eq. (1), with the Monte Carlo (MC) method.

In this approach we follow classical kinetic theory and describe the electron electron interaction as collision of two neutral, hard spheres each with radius r. To account for the charge of the electrons, and thus Coulomb interaction, we set the radii of our considered hard spheres equal to the screening length.

In the following sections, we describe the assumptions and involved physics in more detail, i.e., the average interaction time τ, the total cross section σ_{tot} as well as the energy transfer.

3.1. Average interaction time

According to kinetic theory [21], the average interaction time τ between two successive interactions is computed via

$$\tau = \frac{\lambda}{\langle g \rangle} = \frac{1}{\langle g \rangle \, n_{\mathrm{e}} \sigma_{\mathrm{tot}}} \qquad \text{with} \qquad \lambda = \frac{1}{n_{\mathrm{e}} \sigma_{\mathrm{tot}}}\,, \tag{7}$$

with λ being the mean free path, n_{e} the total electron density and σ_{tot} the total cross section, corresponding to electron-electron interactions. As we assume all electrons to be moving, we apply the average velocity difference $\langle g \rangle$, with $g = |\vec{v}_1 - \vec{v}_2|$, where $\vec{v}_1$ and $\vec{v}_2$ denote pre-collisional velocities of two different electrons.

3.2. Total cross section

In classical kinetic theory, the total cross section for the collision of two hard spheres, each with radius r, is given by $\sigma_{\mathrm{tot}} = 4\pi r^2$ [21]. Usually, the cross section for the collision of two charged particles is infinite due to the infinite range of the Coulomb potential. To tame this problem, screening is taken into account, which leads to a finite interaction range and thus a finite total cross section [22]. In our case, we apply as screening length the inverse of the so-called screening parameter κ [23]

$$\kappa^2 = \frac{e^2 m_\mathrm{e}}{\pi^2 \varepsilon_0 \hbar^2} \int_0^\infty f(k)\,\mathrm{d}k \,. \tag{8}$$

In Equation (8) f denotes the distribution of the average occupancy of state k, usually called distribution function in statistical physics.

To bridge the gap to the electron energy distribution $\rho_\mathrm{e}(\epsilon)$ in the framework of the EMRE, we take into account a dispersion relation $\epsilon(k)$ and density of states $D(\epsilon)$ of a three dimensional free electron gas [24]

$$\epsilon(k) = \frac{\hbar^2 k^2}{2 m_\mathrm{e}} \qquad \text{and} \qquad D(\epsilon) = \frac{m_\mathrm{e}^{3/2}}{\pi^2 \hbar^3} \sqrt{2\epsilon} \,.$$

As a consequence, we can rewrite κ^2 from Equation (8) as

$$\kappa^2 = \frac{e^2}{2\varepsilon_0} \int_0^\infty \frac{\rho_\mathrm{e}(\epsilon)}{\epsilon}\,\mathrm{d}\epsilon \,. \tag{9}$$

The total cross section is then calculated as $\sigma_\mathrm{tot} = 4\pi/\kappa^2$.

3.2.1. Energy Transfer

In the case of a collision the transferred energy $\Delta\epsilon_\mathrm{tr}$ is computed according to

$$\Delta\epsilon_\mathrm{tr} = \epsilon_1' - \epsilon_1 = \frac{1}{2} m_\mathrm{e} \vec{v}_1^{\,2} - \frac{1}{2} m_\mathrm{e} \vec{v}_1^{\,\prime 2} \,, \tag{10}$$

where $\vec{v}_1$ and $\vec{v}_1'$ denote the pre- and post-collisional velocities. Moreover, the post-collisional velocities of both colliding electrons are determined according to

$$\begin{aligned} \vec{v}_1' &= \frac{1}{2}\left(\vec{v}_1 + \vec{v}_2 + g\,\hat{n}\right) \\ \vec{v}_2' &= \frac{1}{2}\left(\vec{v}_1 + \vec{v}_2 - g\,\hat{n}\right) \,, \end{aligned} \tag{11}$$

where $\hat{n}$ is a point on the unit sphere S^2. As such, Eq. 11 determines the set of all allowed post-collisional velocities $\vec{v}_1'$ and $\vec{v}_2'$ regarding energy and momentum conservation. Finally, in accordance with a MC simulation, the post- collisional velocities are chosen randomly, which will be explained in Sec. 4.2.

4. Algorithm

The method we use to solve Eq. (1) is based on the concept of operator splitting. As such, neglecting the term of electron-electron collisions $\dot{n}_i^{\mathrm{e-e}}$ on the RHS of Eq. (1), we solve

$$\frac{d}{dt} n_i = \dot{n}_i^{\mathrm{pi}} + \dot{n}_i^{\mathrm{imp}} + \dot{n}_i^{\mathrm{e-pn}} + \dot{n}_i^{\mathrm{1pht}}$$

deterministically via a traditional ODE time-step. Then the electron-electron collisions are solved stochastically in a separate time-step. These two different steps represent the different contributions from the collaborating authors. The deterministic step was programmed in `FORTRAN` while the stochastic step was programmed in `C++11`. The two steps passed information during each run via a wrapper (see Fig. 1) as described in Sec. 5. To obtain an extra order of accuracy, initial and final times steps of $\Delta t/2$ are taken with the deterministic method before taking the alternating stochastic and deterministic steps of Δt.

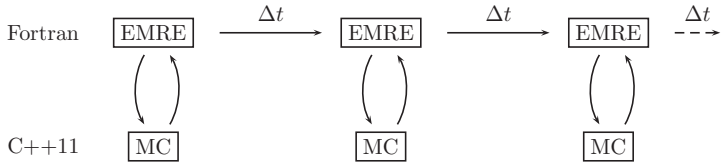

Figure 1: Sketch of the computational interface between the EMRE and MC part programmed in `FORTRAN` and `C++11`, respectively.

4.1. The Deterministic Step

For the deterministic step we use an adaptive step-size Runge-Kutta method to integrate the EMRE over each time step Δt. This returns the distribution $\rho_\mathrm{e}(t,\epsilon)$ at distinct time steps t, evolved by ionization, electron-phonon collisions, and single photon absorption events. The ionization processes increase the number of conduction electrons while the single-photon absorption events drive the system into a strongly non-equilibrium configuration. The alternating Monte-Carlo step, consisting only of electron-electron collisions which change neither the total number of electrons nor the energy of the plasma, plays the major role of driving the system into a quasi-equilibrium state.

4.2. The Stochastic Step

According to the previously described MC method we present the way in which these schemes are combined with the EMRE. The basic idea is that after each time step Δt the EMRE algorithm sends the density distribution $\rho_\mathrm{e}(E)$ to the MC algorithm, which performs the electron electron collisions during Δt and sends the changed distribution back to the deterministic EMRE algorithm.

Initially, the MC algorithm computes the average interaction time τ via the equations (7) and (9). Since the EMRE part provides the electron distribution ρ_e, the total density n_e can be computed according to Eq. (2). Furthermore, the average velocity difference $\langle g\rangle$ is approximated by neglecting the distinction between root mean square (rms) and mean values [25]

$$\begin{aligned}\langle g\rangle \approx g_\mathrm{rms} &= \sqrt{\langle g^2\rangle} = \sqrt{\langle(\vec{v}_1-\vec{v}_2)^2\rangle}\\ &= \sqrt{\langle\vec{v}_1^{\,2}\rangle - 2\langle\vec{v}_1\cdot\vec{v}_2\rangle + \langle\vec{v}_2^{\,2}\rangle}\,,\end{aligned}$$

where we assume the direction to be isotropic and identically distributed. Thus $\langle\vec{v}_1\cdot\vec{v}_2\rangle = 0$ and $\langle\vec{v}_1^{\,2}\rangle = \langle\vec{v}_2^{\,2}\rangle = \langle v^2\rangle$. As a consequence, we proceed with

$$\langle g\rangle \approx \sqrt{2\langle v^2\rangle} = 2\sqrt{\frac{\langle\epsilon\rangle}{m_\mathrm{e}}}\,, \tag{12}$$

where $\langle\epsilon\rangle = \epsilon_\mathrm{tot}/n_\mathrm{e}$ is the average kinetic energy.

The MC algorithm repetitively generates random energies ϵ_1 and ϵ_2 weighted according to the electron distribution $\rho_\mathrm{e}(\epsilon)$ provided by the EMRE part. This is achieved due to inverse transform sampling [26, Chap. 4]. Based on a random energy ϵ, we assume the direction of an electron to be isotropic and thus determine the pre-collisional velocity $\vec{v}$ according to

$$\vec{v} = \sqrt{\frac{2\epsilon}{m_\mathrm{e}}}\begin{pmatrix}\cos\varphi\sin\vartheta\\ \sin\varphi\sin\vartheta\\ \cos\vartheta\end{pmatrix} \qquad \text{with} \qquad \begin{aligned}\varphi &= u_1\cdot 2\pi\\ \vartheta &= \cos^{-1}(2u_2-1)\end{aligned} \tag{13}$$

Algorithm 1 Overview of the combined EMRE and MC methods.

while $t \leq t_{\max}$ **do**
  ▷ start EMRE step
  advance (1) by $\Delta t/2$ via standard ODE integrator
  calculate contributions to (1) by (3), (4), (5), (6)
  ODE integrator provides new $\rho_{\mathrm{e}}(\epsilon)$
  ▷ stop EMRE step
  ▷ start MC step
  advance $\rho_{\mathrm{e}}(\epsilon)$ by Δt via electron-electron collisions
  apply inverse transform sampling to $\rho_{\mathrm{e}}(\epsilon)$
  compute n_{e}, σ_{tot} and $\langle g \rangle$ with (2), (9) and (12)
  compute τ with (7)
  for number of runs N **do**
    sample t_{int}, $\vec{v}_1$ and $\vec{v}_2$ according to (13)
    if $t_{\mathrm{int}} \leq \tau$ **then**
      compute $\vec{v}_1'$, $\vec{v}_2'$ and E_1' and E_2' via (11)
      compute energy transfer according to (10)
    else
      $E_1' \leftarrow E_1$ and $E_2' \leftarrow E_2$
      $\vec{v}_1' \leftarrow \vec{v}_1$ and $\vec{v}_2' \leftarrow \vec{v}_2$
    end if
  end for
  ▷ end MC step
  ▷ continue EMRE step
  advance (1) by $\Delta t/2$ via standard ODE integrator
  calculate contributions to (1) by (3), (4), (5), (6)
  ODE integrator provides new $\rho_{\mathrm{e}}(\epsilon)$
  ▷ end EMRE step
  $t \leftarrow t + \Delta t$
end while

where u_1, $u_2 \in (0, 1)$ are uniformly distributed random numbers. Summarized, we sample the direction as points from the unit sphere S^2 [27].

Furthermore, the interaction time t_{int} is assumed to be exponentially distributed. As a consequence, we sample according to $t_{\mathrm{int}} = -\tau \ln u$, where $u \in (0, 1)$ is a uniformly distributed random number [26, Chap. 4]. Thus, if the sampled interaction time t_{int} is smaller or equal than the provided time step Δt, the two randomly determined electrons collide with each other. In this case, the energy transfer is computed according with Eq. (10) and Eq. (11). Again, in Eq. (11) the point $\hat{n}$ on the unit sphere is uniformly sampled. This describes the fact that, in the case of a collision of hard spheres, the scattering angle is uniformly distributed in $(0, \pi)$ [28].

Let us stress again that we consider a simplified model computing the collision of two neutral hard spheres and account for Coulomb interaction via the screening number κ. As such, the scattering angle is not governed by the differential cross section of Coulomb scattering, *i.e.*, the Rutherford formula.

4.3. The combined steps

To obtain an extra order of accuracy, initial and final time steps of $\Delta t/2$ are taken with the deterministic method before taking the first stochastic step of Δt. After that the steps are taken alternately each over Δt, until the ending deterministic step of $\Delta t/2$. Algorithm 1 provides an overview of the combined EMRE and MC methods presented as a pseudo code.

5. Interface

In this section, the interface between the two programing languages `C++11` and `FORTRAN` 2003 is described. Here the main program to be executed is written in `FORTRAN` 2003 and calls code from `C++11` via a wrapper interface. As has been pointed out above, the Monte Carlo part is written in `C++11`. A major constituent of a Monte Carlo simulation is a random number generator (RNG), which provides random numbers according to a required distribution. Note that the `C++11` standard provides several random number generators as well as distributions. In our case, we choose the Meresenne Twister random number generator [17].

Moreover, the sequence of random numbers is initialized by a seed, which determines the initial state of the RNG engine. This state is updated after each call of a random number. For the sake of good programming style, the RNG shall be initialized once with a fixed seed. This allows reproducing the results corresponding to the Monte Carlo part. As a consequence, we avoid initializing the RNG each time the `FORTRAN` 2003 part calls the MC part by initializing the RNG only once at the beginning of the first calculation. Thus the same random number generator is available throughout the simulation.

In the following, the `intrinsic ISO_C_BINDING` module serves as communication between `FORTRAN` and `C/C++` by binding each `FORTRAN` subroutine to an `external C` function. In our `FORTRAN` 2003 module, a derived data type is initialized, which contains a pointer, able to store the address of a `C/C++` object. In the next step, an external `C` function is called, which initializes a `C++` class, comprising the RNG. The address of this object is stored in the previously denoted pointer. As a consequence, the RNG is initialized with a fixed seed.

From now on, `FORTRAN` 2003 can repeatedly invoke the electron-electron collisions by calling the corresponding `C++` member function via an external `C` function and the stored pointer address. Example code for this interface is provided in the supplementary material.

6. Simulations

We solve Eq. (1) using the algorithm described in Sec. 4. These calculations are performed for ultrashort pulses of three different pulse durations of 15 fs, 30 fs, and 60 fs, as measured by the full width at half the maximum intensity, τ_w. The central wavelength of each pulse is taken to be 400 nm with a peak intensity of $I_0 = 4 \times 10^{17}\,\mathrm{W\,m^{-2}}$. The pulse shape is assumed to be Gaussian and the intensity in each case is given by $I(t) = I_0\,\exp(-4\ln(2)\,t^2/\tau_\mathrm{w}^2)$. Note that by keeping the same peak intensity for each pulse while changing the pulse width for each, we are changing the total pulse energy for each simulation.

The material is assumed to have a band gap of 9 eV and a linear refractive index of $n_0 = 1.47$, like fused silica glass. The electron and hole masses are approximated as equal to the free electron mass. The electron-phonon collision time τ_i^pn and free-carrier momentum scattering time τ_i^c are calculated from the energy and momentum scattering rates as functions of electron energy from Ref. [29]. The average phonon energy is assumed to be $\epsilon^\mathrm{pn} = 33\,\mathrm{meV}$ [30]. In our calculations we set the energy discretization $\Delta\epsilon$ equal to ϵ^pn, yielding a value of $j = 93$ for the photon energy index in Table. 1, and set the maximum EMRE energy index to $m = 1500$. The value for the impact ionization parameter rate is estimated to be $P_\mathrm{imp} = 21.2\,\mathrm{fs^{-1}}$ which was calculated from a Boltzmann collision integral for energies near the critical energy ϵ_c in Ref. [16]. During the simulation, the conduction electron distribution as a function of energy, $\rho_\mathrm{e}(\epsilon)$, and the total ionization yield, n_e, are recorded at each time step. Each simulation was performed once with the electron-electron collisions included and then performed again without this contribution.

7. Results

The laser pulse intensity and resulting ionization yields for each simulation are shown in Fig. 2 as functions of time. Note that although the pulse shape is the same for each plot, the time axes are normalized to the respective pulse width τ_w. Note also that the maximum yields (measured on the left axes) increase with increasing pulse width. Comparison between the curves including (solid blue lines) and excluding (dotted red lines) electron-electron collisions show that for each pulse width the evolution of $n_\mathrm{e}(t)$ prior to the pulse peak is not significantly changed by these collisions. At those earlier times the influence of photo-ionization

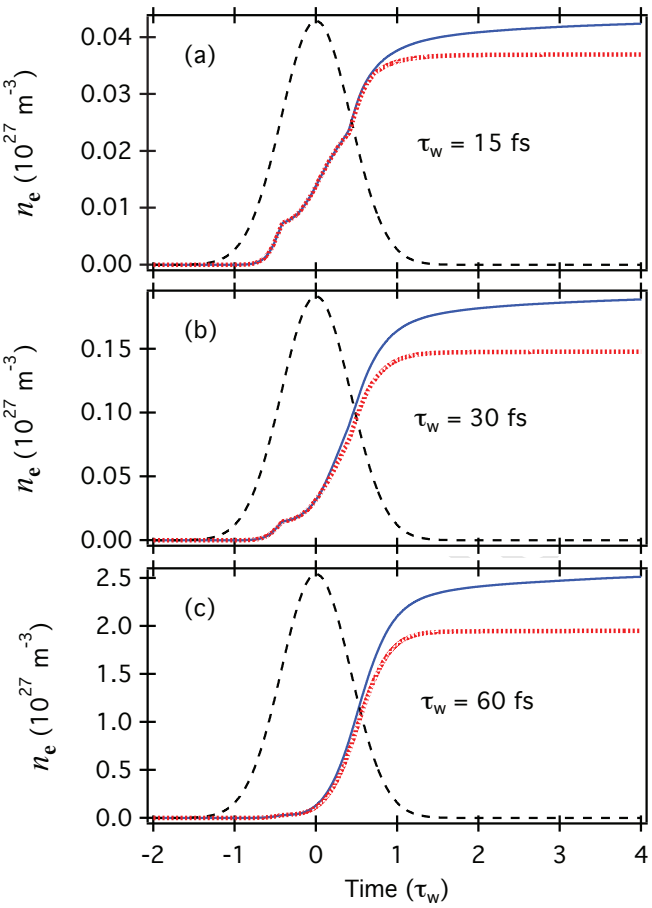

Figure 2: The normalized laser intensity (dashed black line) and total ionization yield, n_{e}, with (solid blue line) and without (dotted red line) electron-electron collisions, shown as functions time for pulses with durations of (a) 15 fs, (b) 30 fs, and (c) 60 fs. The peak intensity of each run was $I_0 = 4 \times 10^{17}\,\mathrm{W\,m^{-2}}$. Note that the time axis is normalized to the pulse width τ_w, while the density axes are rescaled for each panel.

is dominant. Thus one finds a characteristic feature in $n_{\mathrm{e}}(t)$ occurring approximately at $t = -\tau_{\mathrm{w}}/2$ for each simulation. This feature comprises a sudden shift in dn_e/dt resulting from an increase of the number of photons required to overcome the effective band gap during photo-ionization,f as described by the Keldysh model. The opposite of this feature occurs in Fig. 2a at time $t = +\tau_{\mathrm{w}}/2$ when one less photon is required for photo-ionization. Such behavior is also present in Fig. 2b and Fig. 2c, but it is hidden in the data due to the dominating influence of impact ionization over longer times.

Another feature in each plot of Fig. 2 is a continued increase of the conduction band population after the pulse has gone that only occurs when electron-electron collisions are included. This post-pulse increase of the ionization yield stabilizes on the order of a picosecond and increased the total yield between 10 % - 20 %.

For times $t > +\tau_{\mathrm{w}}$ the pulse intensity becomes small. Therefore photo-ionization plays a negligible role at these later times and any significant increase of the ionization yield comes from impact ionization. A more detailed explanation of this behavior is provided by the data in Fig. 3 and Fig. 4. These figures show the corresponding numerical solutions to Eq. (1) (divided by the discretization energy $\Delta\epsilon$) as functions of electron energy and time including (Fig. 3) and excluding (Fig. 4) electron-electron collisions. During these electron-electron collisions the total electron density and energy are conserved. However, the thermalization

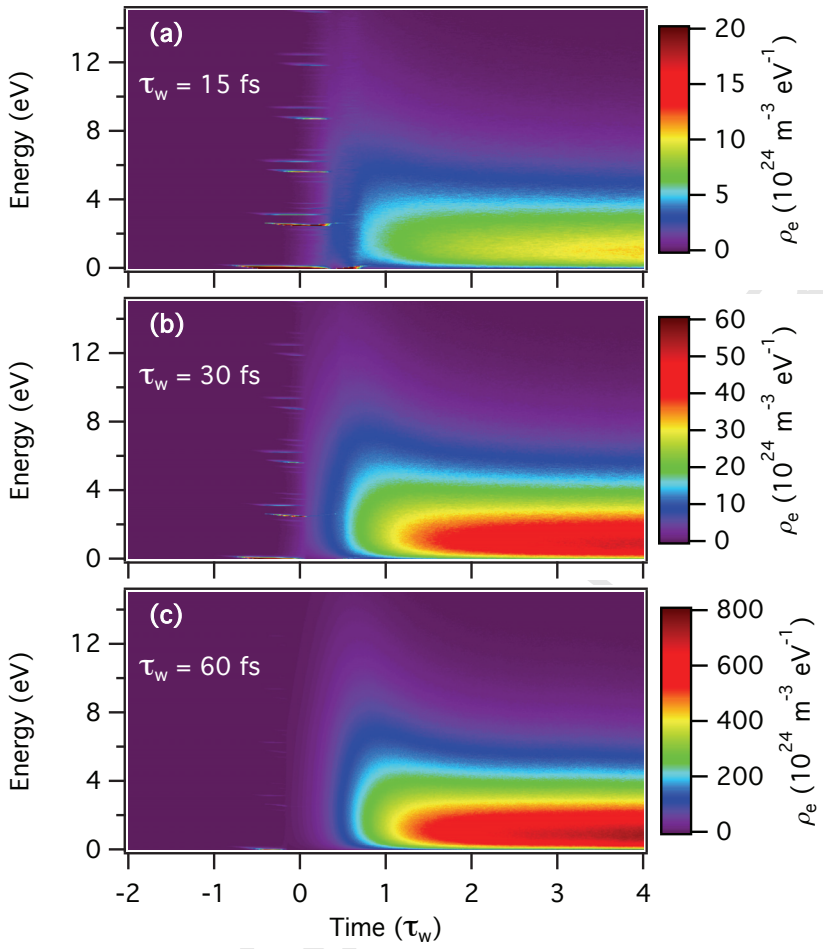

Figure 3: Conduction band electron distributions as functions of energy and time for pulses with durations of (a) 15 fs, (b) 30 fs, and (c) 60 fs. These results include electron-electron collisions.

does cause a small fraction of initially lower-energy electrons to suddenly gain energies high enough for impact ionization ($\epsilon^{\text{crit}} \geq 13.5$ eV in our case) without the need of absorbing additional photons from the laser field. This effect keeps increasing the ionization yield after the pulse has passed.

Figure 3a and 3b, as well as all of Fig. 4 show how the sharp-peaked distribution, prior to the pulse peak for the shortest pulses, thermalizes. These early peaks in the distribution arise from photo-ionization into low energies followed by single photon absorption events to higher energies as described by the MRE. However, the peaks are thermalized rapidly (on the order of 10 fs or less) by the electron-electron collision contributions. Therefore, if one includes electron-electron collisions in the EMRE for the pulses under consideration, only for the 15 fs pulse do these initial distribution peaks remain throughout the pulse duration and thermalize after the pulse is gone (see Fig. 3).

In the results without electron-electron collisions shown in Fig. 4 the distribution maintains a non-equilibrium shape throughout the simulations. Even so, some spreading of the sharp distribution peaks over time still occurs. This thermalization is primarily due to energy loss of electrons into the phonon gas and our EMRE's largely artificial placement of post-impact ionization electrons. If more realistic models of electron-phonon collisions or impact ionization were used, the thermalization in Fig. 4 would likely be greater.

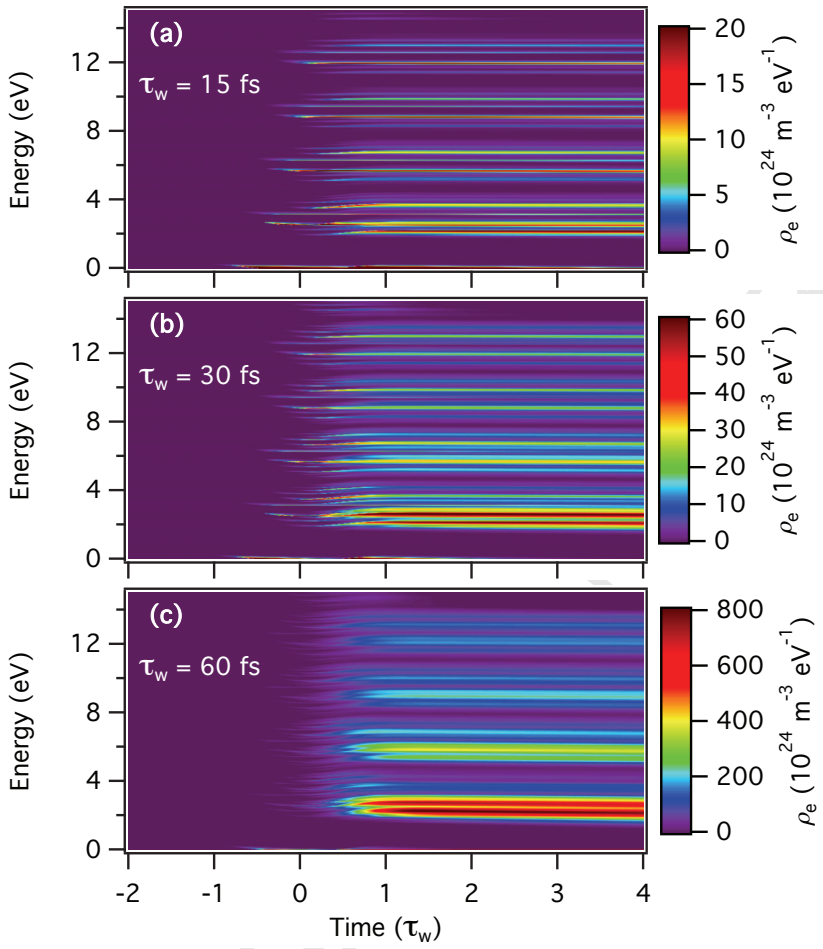

Figure 4: Conduction band electron distributions as functions of energy and time for pulses with durations of (a) 15 fs, (b) 30 fs, and (c) 60 fs. These results neglect electron-electron collisions.

Regardless, comparison of Fig. 3 and Fig. 4 demonstrate that the role of electron-electron collisions in determining the distribution shape is decisive, at least for time scales greater than a few tens of femtoseconds.

In comparing the distribution shapes on the leading and trailing pulse edges, it is helpful to look at 1D plots of the distribution at specific times prior to and after the pulse peak. Numerical solutions to Eq. (1) (again divided by the discretization energy $\Delta\epsilon$) are shown in Figs. 5 and Fig. 6 as functions of electron energy for times surrounding the peak of the laser intensity. Note here, as in the earlier figures, that the maximum distribution values change with changing pulse widths so as to better contrast the respective distribution shapes at the various times. These specific times are also given in units of the pulse width, τ_w.

The important conclusion to draw from these results is that at the peak of the 60 fs pulse, see the $t = 0$ fs plot in Fig. 5 (c), the distribution is already thermalized by electron-electron collisions. This is not the case for the 15 fs and 30 fs pulses in Fig. 5a and Fig. 5b. In many calculations of laser-induced ionization, particularly those used in pulse propagation simulations, the ionization yield is used in combination with a Drude model to simulate the entire response of free charges [6, 7]. Although the peak ionization yields shown in Fig. 2 are of the same order of magnitude whether or not electron-electron collisions are included, comparison of Fig. 5 and Fig. 6 demonstrates the significance of electron-electron collisions to the electron

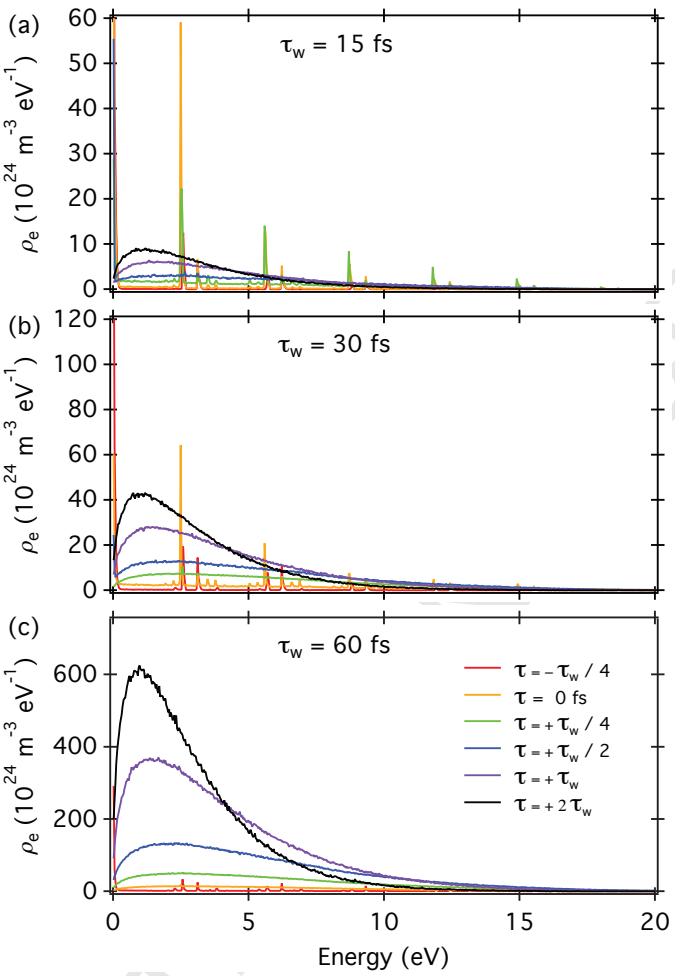

Figure 5: Conduction band electron distributions as functions of energy at various times for pulses with durations of (a) 15 fs, (b) 30 fs, and (c) 60 fs. These results include electron-electron collisions.

distribution shape even for the shortest pulses under consideration. The distinction is not a trivial one for those wishing to interface the laser-material response to pulse propagation simulations. The shape of the electron distribution has a definite effect on the optical properties of the carriers due to the energy dependence of quantities such as momentum and energy relaxation times. This consequence has been demonstrated by theoretical works [14, 29] as well as experimental validation of theoretical treatments using time-dependent reflectivity and absorption measurements [31]. The primary driver of this effect in each case was the non-equilibrium state of the free carriers. Therefore, since many ubiquitous models of free-carrier optical properties assume a thermalized distribution in quasi-equilibrium, they are highly questionable for pulse durations under 50 fs. The presented approach addresses this issue by separating the fast calculations of the EMRE from the more cumbersome thermalizing calculations required for classical electron-electron collision modeling. By doing so, each calculation may be optimized separately from the other.

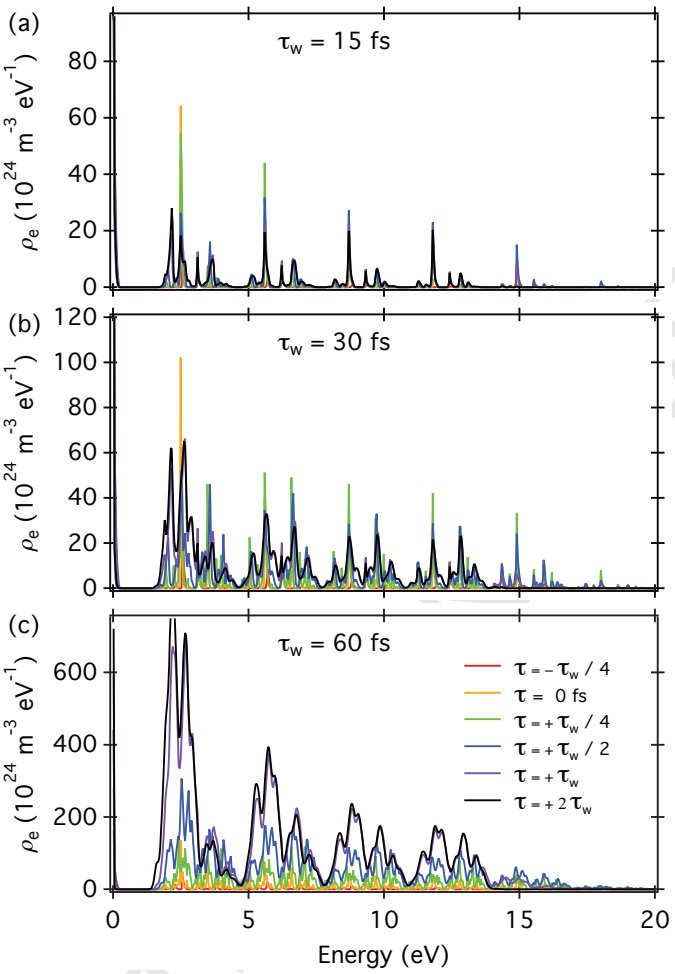

Figure 6: Conduction band electron distributions as functions of energy at various times for pulses with durations of (a) 15 fs, (b) 30 fs, and (c) 60 fs. These results neglect electron-electron collisions.

8. Conclusion

A `C++11` / `FORTRAN` 2003 interface is presented and used to combine deterministic and stochastic methods of modeling electron collisions in solids exposed to ultrashort laser pulses. The presented simulations using this interface evolve the conduction band energy-dependent electron distribution in a dielectric solid exposed to an ultrashort high-intensity laser pulse. The simulations take a split-step approach comprising a stochastic Monte-Carlo step to simulate electron-electron collisions, and a deterministic step solving an extended multi-rate equation with standard ODE solvers for all other collisions. The results show that the model of electron-electron scattering plays a dominant role in the evolution of the electron energy distribution. This has, for instance, consequences on the free-carrier dependence of optical properties.

This approach is advantageous because it separates the fast calculations of the EMRE (typically coupled to the field evolution) from the more demanding calculations required for proper electron-electron collision modeling. Therefore, each calculation may be optimized separately from the other. This technique is ideal for simulations of high-intensity, long distance pulse propagation in solids, which requires simultaneous modeling of the field and material evolution.

Acknowledgements

The authors gratefully acknowledge partial support of this research by the Carl Zeiss foundation, by the Deutsche Forschungsgemeinschaft under grant number RE 1141/15, and by the Air Force Office of Scientific Research under Contract No. FA9550-13-1-0069.

References

[1] P. Balling, J. Schou, Femtosecond-laser ablation dynamics of dielectrics: basics and applications for thin films, Rep. on Prog. in Phys. 76 (2013).
[2] A. Vogel, J. Noack, G. Huttman, G. Paltauf, Mechanisms of femtosecond laser nanosurgery of cells and tissues, Appl. Phys. B 81 (2005) 1015–1047.
[3] P. Hannaford (Ed.), Femtosecond Laser Spectroscopy, Springer Science Business Media, Inc., 2005.
[4] R. W. Boyd, Nonlinear Optics, 2nd ed., Academic Press, 2002.
[5] R. L. Sutherland, Handbook of Nonlinear Optics, 2nd ed., Dekker, New York, 2003.
[6] L. Bergé, S. Skupin, R. Nuter, J. Kasparian, J.-P. Wolf, Ultrashort filaments of light in weakly ionized, optically transparent media, Rep. on Prog. in Phys. 70 (2007) 1633.
[7] A. Couairon, E. Brambilla, T. Corti, D. Majus, O. de J. Ramírez-Góngora, M. Kolesik, Practitioner's guide to laser pulse propagation models and simulation, Eur. Phys. J. 199 (2011) 5–76. 10.1140/epjst/e2011-01503-3.
[8] E. Lorin, S. Chelkowski, A. Bandrauk, A numerical maxwell–schrödinger model for intense laser–matter interaction and propagation, Comput. Phys. Commun. 177 (2007) 908 – 932.
[9] C. Karle, J. Schweitzer, M. Hochbruck, K. Spatschek, A parallel implementation of a two-dimensional fluid laser–plasma integrator for stratified plasma–vacuum systems, J. of Comput. Phys. 227 (2008) 7701 – 7719.
[10] S. Mauger, G. C. de Verdière, L. Bergé, S. Skupin, Gpu accelerated fully space and time resolved numerical simulations of self-focusing laser beams in sbs-active media, J. Comput. Phys. 235 (2013) 606 – 625.
[11] R. Fischer, A. Staudt, C. Keitel, Simulation of atomic quantum dynamics in combined intense laser and weak electric fields, Comput. Phys. Commun. 157 (2004) 139 – 146.
[12] B. Rethfeld, Unified model for the free-electron avalanche in laser-irradiated dielectrics, Phys. Rev. Lett. 92 (2004) 187401.
[13] N. Medvedev, B. Rethfeld, A comprehensive model for the ultrashort visible light irradiation of semiconductors, J. Appl. Phys. 108 (2010) 103112.
[14] J. R. Gulley, T. E. Lanier, Model for ultrashort laser pulse-induced ionization dynamics in transparent solids, Phys. Rev. B 90 (2014) 155119.
[15] C. Wang, T. Lin, R. Caflisch, B. I. Cohen, A. M. Dimits, Particle simulation of Coulomb collisions: Comparing the methods of Takizuka & Abe and Nanbu, J. Comput. Phys. 227 (2008).
[16] A. Kaiser, B. Rethfeld, M. Vicanek, G. Simon, Microscopic processes in dielectrics under irradiation by subpicosecond laser pulses, Phys. Rev. B 61 (2000).
[17] M. Matsumoto, T. Nishimura, Mersenne Twister: A 623-dimensionally Equidistributed Uniform Pseudo-random Number Generator, ACM Trans. Model. Comput. Simul. 8 (1998) 3–30.
[18] B. Rethfeld, Free-electron generation in laser-irradiated dielectrics, Phys. Rev. B 73 (2006) 035101.
[19] L. V. Keldysh, Ionization in the field of a strong electromagnetic wave, Sov. Phys. JETP 20 (1965) 1307.
[20] B. Christensen, P. Balling, Modeling ultrashort-pulse laser ablation of dielectric materials, Phys. Rev. B 79 (2009).
[21] D. R. Nicholson, Introduction to Plasma Theory (Plasma Physics), Wiley, 1983.
[22] M. Mitchner, C. H. Kruger, Partially ionized gases, Wiley, New York, 1973.
[23] R. Binder, H. S. Köhler, M. Bonitz, N. Kwong, Green's function description of momentum-orientation relaxationof photoexcited electron plasmas in semiconductors, Phys. Rev. B 55 (1997) 5110–5116.
[24] N. W. Ashcroft, N. D. Mermin, Solid State Physics, Cengage Learning, 1976.
[25] F. Reif, Fundamentals of Statistical and Thermal Physics, Waveland Pr Inc, 2008.
[26] T. Müller-Gronbach, E. Novak, K. Ritter, Monte Carlo-Algorithmen, Berlin: Springer, 2012.
[27] C. Graham, D. Talay, Stochastic simulation and Monte Carlo methods. Mathematical foundations of stochastic simulation, Berlin: Springer, 2013.
[28] M. A. Lieberman, A. J. Lichtenberg, Principles of Plasma Discharges and Materials Processing , 2nd Edition, Wiley-Interscience, 2005.
[29] D. Arnold, E. Cartier, D. J. DiMaria, Acoustic-phonon runaway and impact ionization by hot electrons in silicon dioxide, Phys. Rev. B 45 (1992) 1477.
[30] B. C. Stuart, M. D. Feit, S. Herman, A. M. Rubenchik, B. W. Shore, M. D. Perry, Nanosecond-to-femtosecond laser-induced breakdown in dielectrics, Phys. Rev. B 53 (1996) 1749–1761.
[31] J. P. Colombier, P. Combis, E. Audouard, R. Stoian, Transient optical response of ultrafast nonequilibrium excited metals: Effects of electron-electron contribution to collisional absorption, Phys. Rev. E 77 (2008) 036409.